JGR Space Physics

RESEARCH ARTICLE
10.1029/2019JA026864

WINDII Observations and WACCM-X Simulations of High-Latitude Winds Under Different Solar Radio Flux and Geomagnetic Disturbance Conditions

Shushi Liu[1,2,3], Gordon G. Shepherd[3], Yongsheng Chen[3], Marianna G. Shepherd[3], and Sangay Bhutia[3]

[1]Beijing Aerospace Control Center, Beijing, China, [2]Science and Technology on Aerospace Flight Dynamics Laboratory, Beijing, China, [3]Centre for Research in Earth and Space Science, York University, Toronto, Canada

Key Points:
- There are strong westward winds at 140 to 250 km altitude between 100° to 200° longitude and 60° to 70° southern latitude
- WINDII observations and WACCM-X simulations agree well in describing the high-latitude wind
- The strong zonal westward wind magnitude depends on the solar radio flux and geomagnetic activity

Correspondence to:
S. Liu,
lss_880211@aliyun.com

Citation:
Liu, S., Shepherd, G. G., Chen, Y., Shepherd, M. G., & Bhutia, S. (2019). WINDII observations and WACCM-X simulations of high-latitude winds under different solar radio flux and geomagnetic disturbance conditions. *Journal of Geophysical Research: Space Physics*, *124*, 6087–6096. https://doi.org/10.1029/2019JA026864

Received 21 APR 2019
Accepted 20 JUN 2019
Accepted article online 4 JUL 2019
Published online 13 JUL 2019

Abstract Thermospheric zonal winds at altitudes of 140 to 250 km are shown to reverse from eastward to strong westward between 100° and 200° in geographic longitude and 60°S to 70°S latitude in the Southern Hemisphere. The reversal also occurs at the same latitude in the Northern Hemisphere, but from 200° to 340° longitude. The phenomenon has been previously described as a "wind wall." Observations by the Wind Imaging Interferometer (WINDII) on the National Aeronautics and Space Administration's Upper Atmosphere Research Satellite (UARS) and simulations by the Whole Atmosphere Community Climate Model with thermosphere and ionosphere extension (WACCM-X) are utilized to explore the characteristics of what has been called a wind wall. In order to study the dependence on solar radio flux and geomagnetic activity, the relationships of the maximum zonal wind and F10.7 (the solar radio flux at 10.7 cm) and ap indices are investigated. The results show that WINDII observations and WACCM-X simulations agree well in describing this wind signature. Moreover, the appearance of the wind wall is found to have a strong dependence on the solar radio flux and geomagnetic activity. In addition, WINDII winds have a stronger response to geomagnetic activity than WACCM-X winds.

1. Introduction

Thermospheric neutral wind circulation at high latitudes is attracting more and more attention from space weather scientists, primarily because neutral winds are predominantly coupled to the ionospheric convecting plasma via momentum exchange between ions and neutrals (Richmond et al., 2003; Kwak & Richmond, 2007; Dhadly et al., 2018.) High-latitude thermospheric winds are forced mainly by solar irradiance, atmospheric tides, waves propagating from below, momentum transfer between ions and neutrals, and internal small-scale instabilities (Kwak & Richmond, 2014).

There has been a significant number of theoretical and experimental studies of high-latitude neutral winds. Richmond et al. (2003) statistically analyzed Wind Imaging Interferometer (WINDII) observations at high southern latitudes in magnetic coordinates and correlated these with the interplanetary magnetic field (IMF) to determine the influence of IMF-dependent ionospheric convection on the winds. They found the velocity of the averaged neutral wind in the polar cap often exceeds 300 m/s. Emmert et al. (2008) and Drob et al. (2008) presented a global empirical disturbance wind model (DWM07), which shows that average wind disturbances at high latitude reach magnitudes in excess of 300 m/s for Kp = 7. Kwak and Richmond (2014) analyzed the vertical component of vorticity and the horizontal divergence of the high-latitude neutral wind field in the lower thermosphere during southern summer for different IMF conditions with the aid of the TIEGCM model. Zhang and Shepherd (2008) described "extreme longitudinal disturbances" in WINDII winds, on days in March 1994, 1996, and 1997. The disturbed zonal and meridional winds were found at 40°S latitude between 100° and 200° longitude. Huang et al. (2017) investigated the relationship between high-latitude ionospheric currents and thermospheric wind from Challenging Mini-satellite Payload (CHAMP) observations. Their results indicated that the plasma drift and the neutral forces were of comparable influence on the zonal wind at the CHAMP altitude (initial altitude of 454 km) in the noon sector.

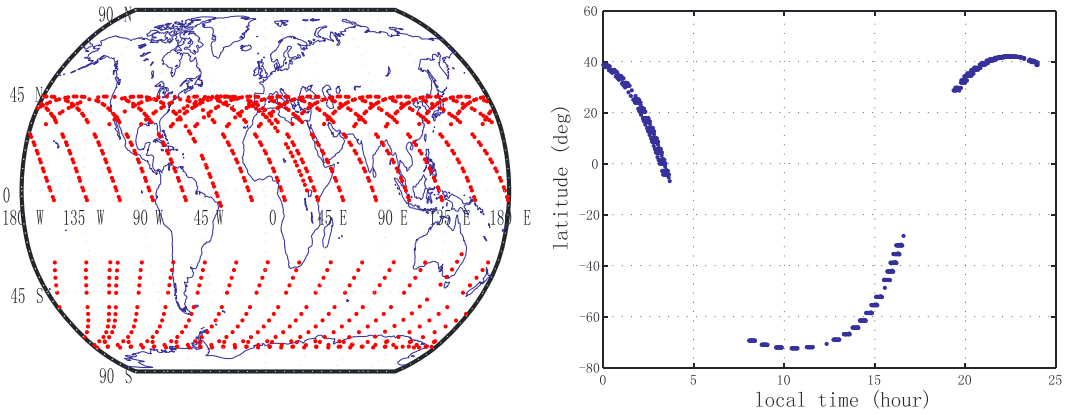

Figure 1. Coverage of Wind Imaging Interferometer observations for 3 February 1992, in longitude and latitude (left) and local time and latitude (right).

By exploring WINDII observations, Shepherd and Shepherd (2018) reported a zonal wind phenomenon they called a "wind wall." When the WINDII high-latitude thermospheric zonal wind data near local noon were investigated, reversals in the wind direction were observed at altitudes of 140 to 250 km from eastward to westward at geographic latitudes between 60° and 70°. The strong westward winds were confined to a narrow region between 100° and 200° in longitude in the Southern Hemisphere and at 200–300° in the Northern Hemisphere. The westward velocities reached 400 m/s, and even 600 m/s, within a background of much smaller eastward winds at all other longitudes.

In this paper, these previous studies (Shepherd & Shepherd, 2018; Zhang & Shepherd, 2008) have been extended by a systematic analysis of the solar input influence on the wind wall. On the basis of numerical simulations using the Whole Atmosphere Community Climate Model with thermosphere and ionosphere extension (WACCM-X) model, a comparative analysis of the response of the strongest westward wind on a given day to the F10.7 solar radio flux and the geomagnetic variations for that day was conducted. To our knowledge, no such systematic comparison of WACCM-X simulations to neutral wind observations has previously been carried out. The WINDII observations and WACCM-X model are described in section 2, followed by the discussion of results in section 3, and the conclusions are presented in section 4.

2. Descriptions of WINDII and WACCM-X

2.1. WINDII Data

WINDII is a limb scanning Michelson interferometer, which was launched on the Upper Atmosphere Research Satellite (UARS) satellite on 12 September 1991. WINDII produced wind, temperature, and airglow emission rate over an altitude range of 80–300 km. Height profiles of horizontal winds were derived from line-of-sight wind measurements in two fields of view placed at 45° and 135° to the UARS velocity vector. The two fields of view sampled the same atmospheric volume within about 8 min of each other (Shepherd et al., 1993, 2012). UARS was in a 57° inclination orbit, and because of the sideways viewing, the WINDII observations extended to 72° geographic latitude. The orbital period of UARS was 96 min, and the precession rate was 5° per day, so that all local times were sampled every 36 days. A yaw maneuver was performed every 36 days to allow the limb scanning instruments to view alternately from 72°S/42°N to 42°S/72°N throughout the course of the year. Figure 1 shows the longitude versus latitude coverage and local time versus latitude coverage of WINDII observations for one day, taking 3 February 1992, for example. At 45°N to 72°S latitude, these observations covered almost all longitudes and 1–24 hr local time, but only around 8–15 hr LT for the high latitudes (60–72°S).

The present study uses zonal wind data over the 90- to 250-km altitude range from the atomic oxygen O (^{1}S) 557.7-nm daytime airglow emission. Typical daytime wind errors were estimated to be 5–7 m/s at 100–160 km heights, increasing to 17 m/s at 200 km (Gault et al., 1996). The wind velocities at the wall boundary are 200–400 m/s; therefore, WINDI observations allow the description of wind wall events with good precision.

Table 1
Cases Under Different Geomagnetic Conditions

Date	F10.7	Max. ap	Daily ap	Mini. Dst	Latitude coverage
High F10.7 and geomagnetically quiet period					
1992-02-11	218.4	9	6.9	−46	60–70°S
High F10.7 and geomagnetically active period					
1992-02-02	280.1	94	56.3	−143	60–70°S
1992-02-03	263.2	179	91.8	−170	60–70°S
Low F10.7 and geomagnetically active period					
1992-05-09	129.2	111	32.7	−37	60–70°N
1992-05-11	128.8	154	69.9	−169	60–70°N
Low F10.7 and geomagnetically quiet period					
1995-03-21	89.3	4	2.1	−16	60–70°S
1995-12-13	70.4	5	1.9	−12	60–70°N
1995-12-18	66.4	5	3.3	−19	60–70°N

Note. The 10.7-cm solar radio flux (F10.7), the maximum geomagnetic index ap (Max. ap), the averaged ap (Daily ap), and the minimum Dst index (Mini. Dst) within 1 day are shown, along with the latitude coverage.

2.2. WACCM-X Model

WACCM-X is a comprehensive numerical model, which produces neutral atmospheric 3-D temperature, density, wind, composition, ionospheric parameters, and electric potential fields. It is a part of the NCAR Community Earth System Model (Hurrell et al., 2013) and extends the description of the neutral atmosphere to altitudes as high as between 500 and 700 km. As a part of Community Earth System Model, WACCM-X is coupled to the dynamic or specified ocean, land, and ice model components. The simulations employed here use a horizontal resolution of 1.9° in latitude and 2.5° in longitude, and the vertical resolution of 0.25 scale heights above 1 hPa. The chemical, dynamical, and physical processes in the troposphere, stratosphere, and mesosphere are based on those in the regular WACCM4 (Marsh et al., 2013), which itself is based on the CAM4 (Neale et al., 2013). The thermospheric and ionospheric components of WACCM-X add neutral species composition, electron and ion density, and both ion and electron temperatures. The most notable changes are fully coupled low- and middle-latitude electrodynamics, dynamical transport of O^+, and high-latitude forcing by the magnetospheric electric fields as well as specific heat (Liu et al., 2018). Solar irradiance is parameterized using specified extreme ultraviolet and X-ray irradiance from 0.05 to 121 nm, which takes as input the F10.7 and F10.7a (81 days average F10.7; Solomon & Qian, 2005). The effects of geomagnetic activity are incorporated in WACCM-X by applying the Heelis empirical convection pattern (Heelis et al., 1982), which is based on the geomagnetic Kp index.

WACCM-X can be used either for free-running climate simulations (lower atmosphere unconstrained) or with the tropospheric and stratospheric dynamics constrained by meteorology, which is named the "specified-dynamics" or SD version of the model. The Meteorological data from the Modern-Era Retrospective Analysis for Research and Applications include temperature, zonal, and meridional winds up to ~50 km (Rienecker et al., 2011). In the present study, WACCM-X is employed in the SD configuration using Modern-Era Retrospective Analysis for Research and Applications 2 with a 50-hr relaxation time. As a component of the Community Earth System Model, WACCM-X source code and results (2000–2014) are publicly available at the NCAR website. For the simulations of data before the year 2000, the model was run on the Niagara supercomputer of SciNet (https://www.scinethpc.ca/niagara/).

3. Results

3.1. Wind Patterns

Eight cases are investigated under four different geomagnetic conditions, that is, (1) high solar radio flux (F10.7) and geomagnetically quiet period, (2) high F10.7 and geomagnetically active period, (3) low F10.7 and geomagnetically active period, and (4) low F10.7 and geomagnetically quiet period. Table 1 lists the F10.7, Ap, and Dst along with the latitude coverage.

The character of the wind wall is illustrated in Figure 2 for a high F10.7 and geomagnetically quiet period, showing zonal wind as a function of longitude and altitude for a local time near noon and latitude band 60–70°S on 11 February 1992 (day of year [DOY] 92042), when the F10.7 is 218.4 and the Ap is 6.9. Note that by convention the eastward wind is positive, while the westward wind is negative. Figure 2a shows the wind from WINDII observations, which cover the altitude range from 90 to 250 km. WACCM-X simulations at the same time and location as WINDII observations are shown in Figure 2b. Both WINDII and WACCM-X show the narrow vertical blue band (the wall) of strong westward wind at longitude 100–180°, extending from altitude 250 km down to about 120 km. In the wall, the westward wind is as strong as −200 m/s, against a background of wind velocity close to zero.

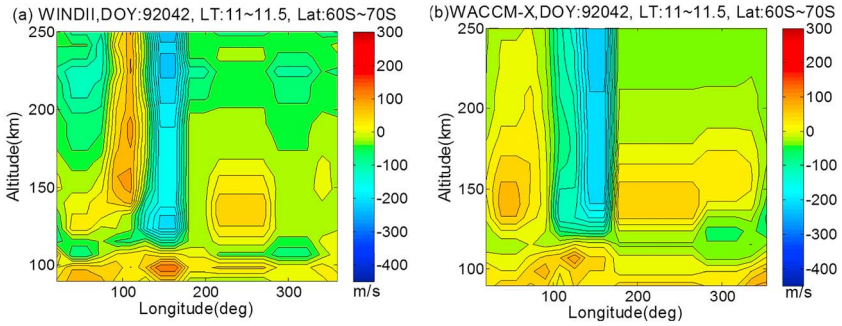

Figure 2. (a) Wind Imaging Interferometer (WINDII) and (b) Whole Atmosphere Community Climate Model with thermosphere and ionosphere extension (WACCM-X) zonal wind shown as altitude versus longitude for high F10.7 and a geomagnetically quiet period on 11 February 1992. DOY = day of year.

Figure 3 shows the same format as Figure 2, but for high solar irradiance and geomagnetically active periods on 2 and 3 February 1992. The wind wall is apparent in both WINDII observations and WACCM-X simulations. WINDII appears to have two wall patterns that are more complex than the WACCM-X simulations. The clear boundary of the wall appears at longitude 200–230°. However, the longitude coverage of strong westward wind, namely, the width of the wall, is quite different. For WINDII, the strong westward wind extends from longitude 50–250° while for WACCM-X it is confined to a narrow longitude band of 150–200°. Moreover, the wind magnitudes are different. The zonal wind velocities from WINDII reach up to −600 m/s while they are about −300 m/s for WACCM-X. The westward wind in the wall in Figure 3 is much stronger than that in Figure 2 while the background wind is similar. Especially for WINDII observations, the strongest wind velocities on Day 33 of 1992 (DOY 92033) are four times larger than those on DOY 92042 (Figure 2). The F10.7 values are both high on the two days, that is, the F10.7 values are 263.2 and 218.4 on DOYs 92034 and 92042, respectively. At the same time, the Ap on DOY 92034 is 12 times larger than the latter. It illustrates that the magnitude of the westward wind has a strong relationship with the geomagnetic activity. However, comparing Figures 3a and 3c, namely, WINDII observations on DOYs 92033 and 92034, the westward wind in Figure 3a is a little larger than that in Figure 3c, although the geomagnetic

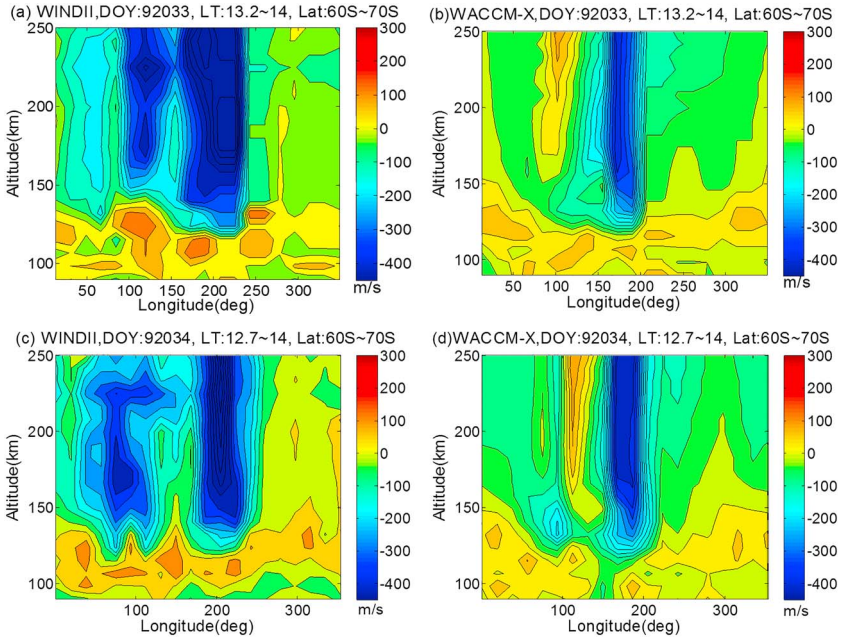

Figure 3. (a and c) Wind Imaging Interferometer (WINDII) and Whole Atmosphere Community Climate Model with thermosphere and ionosphere extension (b and d) (WACCM-X) zonal wind shown as altitude versus longitude for high F10.7 and geomagnetically active periods on (a and b) 2 and (c and d) 3 February 1992.

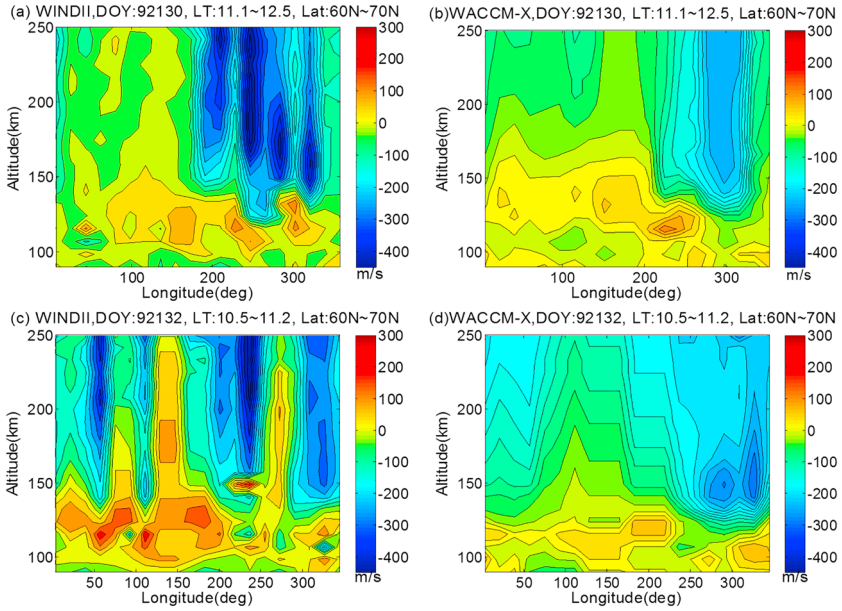

Figure 4. (a and c) Wind Imaging Interferometer (WINDII) and (b and d) Whole Atmosphere Community Climate Model with thermosphere and ionosphere extension (WACCM-X) zonal wind shown as altitude versus longitude for low F10.7 and geomagnetically active periods on (a and b) 9 and (c and d) 11 May 1992. DOY = day of year.

activity of the latter is greater than that of the former (Ap are 91.8 vs. 56.3), with similar F10.7 values. For WACCM-X simulations, Figures 3b and 3d, the westward wind increases as the Ap increases.

The zonal wind in the Northern Hemisphere during low solar irradiance and geomagnetically active periods is illustrated in Figure 4. As opposed to the Southern Hemisphere, the wall is located mainly between 200° and 300° longitudes as noted by Shepherd and Shepherd (2018). The width of the wall from WINDII is wider than that from WACCM-X, as was the case for the results shown in Figure 3. For WINDII observations on DOY 92130, the wind wall extends between the longitudes of 180° and 340°, while it is confined to longitudes around 300° for WACCM-X. For DOY 92132, westward winds dominate both for WINDII observations and WACCM-X simulations, but the WINDII pattern in Figure 4c is more like a Wave 4 while for WACCM-X the wall is weakly evident. Cho and Shepherd (2015) resolved Wave 4 nonmigrating tidal winds with WINDII zonal wind, but for equatorial and midlatitudes. It is worth noting that the local time is between 10.5 and 11.2 hr, which is a little separated from actual noon (12:00–14:00). As the wind wall often appears near noon local time, local time may be the reason why the wind wall is not clearly shown in Figures 4c and 4d. It is also possible that the Northern Hemisphere has some differences from the Southern Hemisphere. Even so, the strongest westward winds from WINDII and WACCM-X locate between the longitudes of 200°–250° and 250–350°, respectively, as Shepherd and Shepherd (2018) described for the wind wall in the Northern Hemisphere.

The F10.7 flux for DOYs 92130 and 92132 are very similar, 129.2 and 128.8, respectively, which isolates the effects of geomagnetic activity on the westward wind. The Ap and minimum Dst are 32.7 and −37, respectively, on DOY 92130, while they are 69.9 and −169 on DOY 92132. However, the strongest westward wind for the Ap of 69.9 is a bit less than that for an Ap of 32.7. There seem to be other factors in controlling the wind wall other than the solar radio flux and geomagnetic activity. Kwak and Richmond (2014) and Huang et al. (2017) described the influence of the IMF on high-latitude thermospheric winds, with winds increasing for negative *By* and *Bz*. The IMF may be the main factor controlling the wind for these days. Unfortunately, the IMF data for the early years are incomplete, and the data for these days are missing.

Figure 5 shows the zonal wind during low solar radio flux and geomagnetically quiet periods when the F10.7 is below 90 and Ap is no larger than 4. On DOY 95080 shown in Figures 5a and 5b, the wind wall is weak and the maximum wind velocities are only −100 m/s. On DOYs 95347 and 95352 shown in Figures 5c–5f, neither WINDII nor WACCM-X presents an evident wall. There are only sporadic westward winds exceeding −100

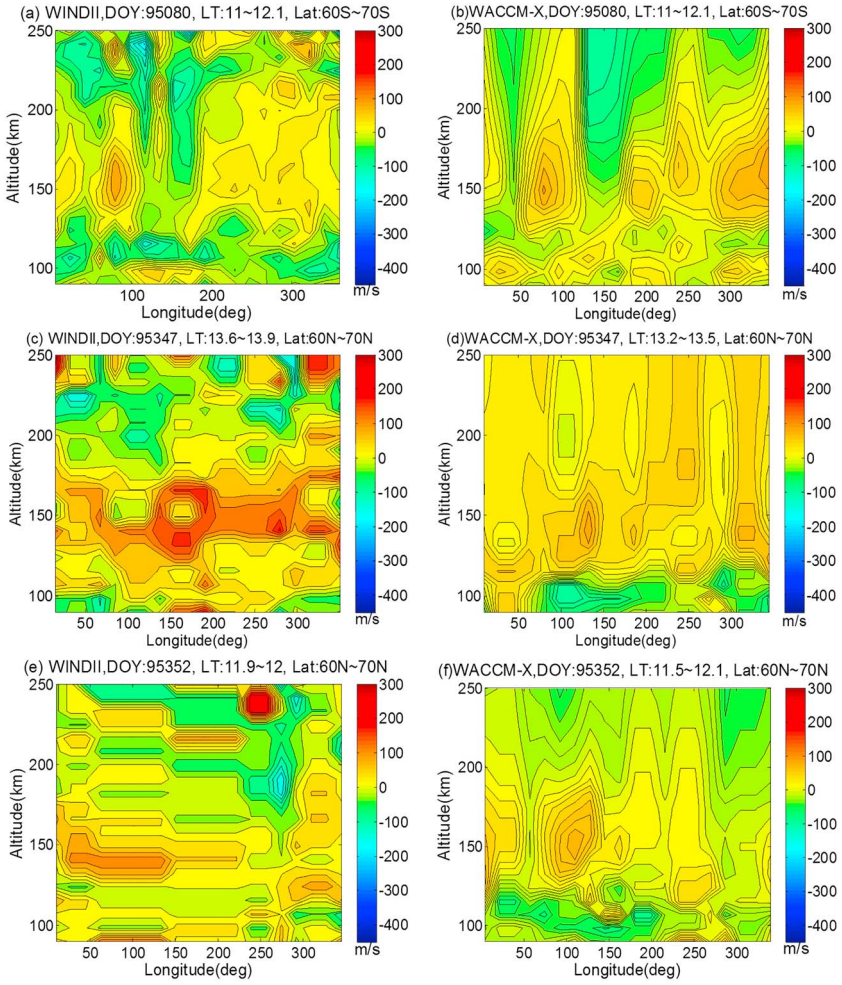

Figure 5. (a, c, and e) Wind Imaging Interferometer (WINDII) and (b, d, f) Whole Atmosphere Community Climate Model with thermosphere and ionosphere extension (WACCM-X) zonal wind shown as altitude versus longitude for low F10.7 and geomagnetically quiet periods on (a and b) 21 March, (c and d) 13, and (e and f) 18 December 1995. DOY = day of year.

m/s above altitude of 180 km in WINDII observations shown in Figures 5c and 5e. For DOY 95080 shown in Figures 5a and 5b, there is a weak wall of around −100 m/s clearly evident for both WINDII and WACCM-X.

3.2. Dependence of the Wind Wall on F10.7 and Ap

9 May 1992 (DOY 92130) is a remarkable day, as all of ap, *By*, and *Bz* begin to increase early in the day and peak just toward the end of the day, so this day is selected to explore the influence of hourly IMF and ap. Figure 6 shows the zonal wind from 90 to 250 km at 60–70°N, in the Northern Hemisphere on DOY 92130 as a function of universal time for WINDII (Figure 6a), WACCM-X (Figure 6b), the *By* and *Bz* hourly values (Figure 6c), and the 3-hourly values of ap (Figure 6d). The WACCM-X simulation is fairly normal, but with high winds, about −300 m/s, while the WINDII winds are around −400 m/s and are split into two components.

Figure 7 shows the diurnal variation of zonal wind as a function of universal time and altitude in the Southern Hemisphere on DOYs 92033 and 92034 and in the Northern Hemisphere on DOY 92132, as well as 3-hourly ap during geomagnetically active periods. During DOY 92033 UT 00:00–05:00, ap reaches 60–80, and WINDII winds exceed −400 m/s. Ap peaks at UT 20:00–24:00, and WINDII winds reach another peak at UT 22:00 (see Figure 7a). WACCM-X simulations show strong westward winds only early in the day (see Figure 7d). On DOY 92034, WINDII winds also present a good correlation with Ap (see Figure 7b) while WACCM-X winds are strongly westward only in the first 5 hr (see Figure 7e). DOY 92132 is different from

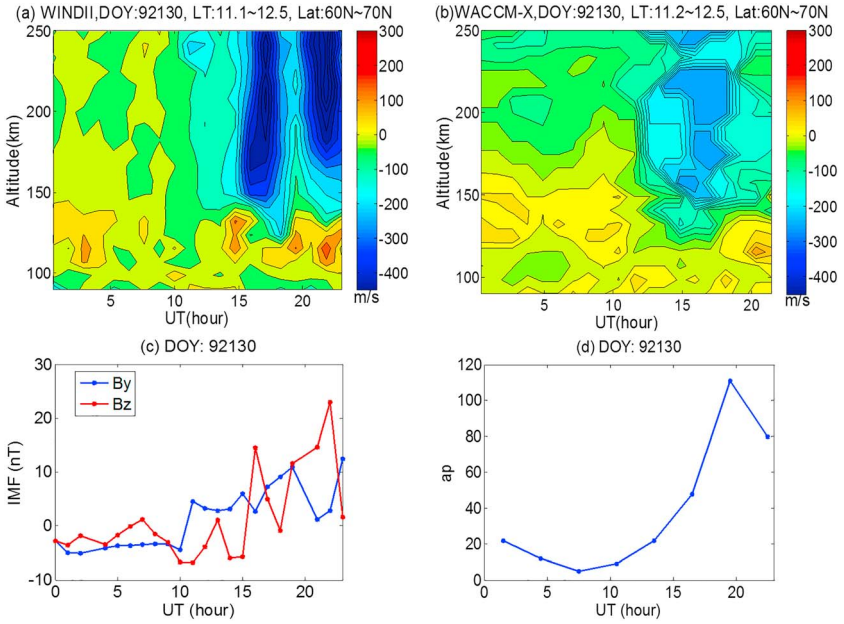

Figure 6. (a) Wind Imaging Interferometer (WINDII) and (b) Whole Atmosphere Community Climate Model with thermosphere and ionosphere extension (WACCM-X) zonal wind shown as altitude versus UT, and variations of IMF (c) and ap (d) on 9 May 1992. DOY = day of year.

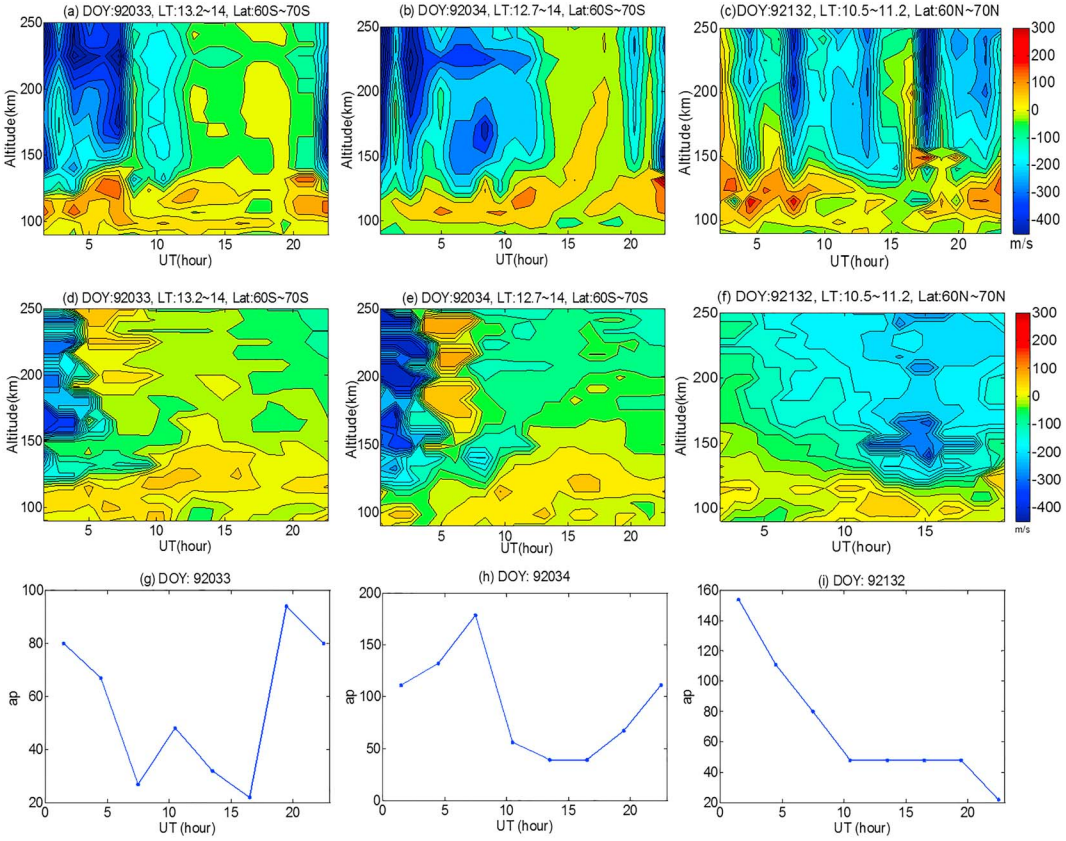

Figure 7. Wind Imaging Interferometer (a, b, and c, upper row) and Whole Atmosphere Community Climate Model with thermosphere and ionosphere extension (d, e, and f, middle row) zonal wind shown as altitude versus UT, and variations of ap (g, h, and i, lower row) on 2 and 3 February 1992 and 11 May 1992. DOY = day of year.

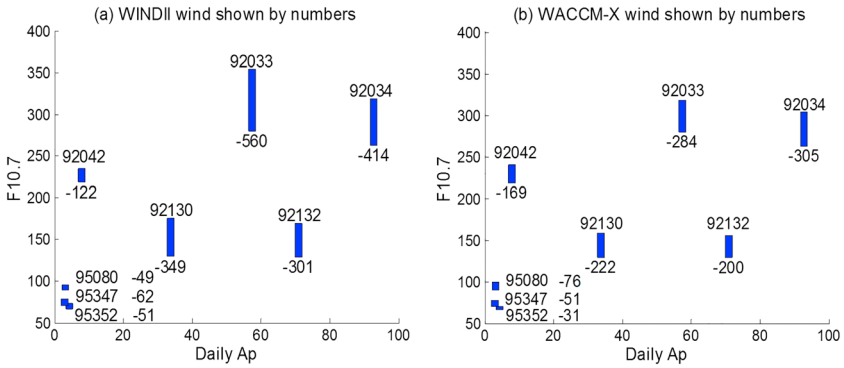

Figure 8. The maximum westward wind at 200 km altitude shown as daily ap versus F10.7 for (a) Wind Imaging Interferometer (WINDII) and (b) Whole Atmosphere Community Climate Model with thermosphere and ionosphere extension (WACCM-X). F10.7 and Ap are shown by the coordinates at the bottom of the bar.

other days. Ap is falling during the whole day while WINDII winds show a wave pattern (see Figure 7c). WACCM-X simulations show no correlation with Ap, and the winds become strong as Ap decreases (see Figure 7f). Neither WINDII nor WACCM-X show an obvious wind wall on this day.

The joint dependence of the wind wall on F10.7 and Ap is investigated in the following part. The zonal wind curves at 200 km altitude as a function of longitude are smoothed separately by 3-point averaging around the nearest longitude. Then for each day the maximum value of each curve is plotted as a function of Ap and F10.7, as shown in Figure 8. The length of the vertical bar represents the wind magnitude, and the values and DOY are shown next to the bars. The coordinates at the bottom of the bar represent the values of F10.7 and Ap. When the solar radio flux and geomagnetic activity are quite low, the (negative) maximum of westward wind does not exceed −100 m/s, and no wind wall appears both for WINDII and WACCM-X, as shown at the bottom left of Figure 8 (DOYs 95080, 95347, and 95352). As the F10.7 increases to 218.4 and Ap is still quiet (DOY 92042), the maximum winds of WINDII and WACCM-X are −122 and −169 m/s, respectively. For the high F10.7 and geomagnetically active periods on DOYs 92033 and 92034, the maximum winds of WINDII reach −560 and −414 m/s, and they are −284 and −305 m/s for WACCM-X.

The F10.7 values are similar while Ap are 32.7 and 69.9, respectively, on DOYs 92130 and 92132. However, both the WINDII and WACCM-X maximum wind on DOY 92132 is weaker than that on DOY 92130, not increasing with Ap. A similar relationship also exists for DOYs 92033 and 92034. Overall, DOYs 92130, 92132, 92033, and 92034 show increasing wind values with increasing F10.7 and Ap, but with some scatter. However, the scatter is the same for WINDII and WACCM, therefore implying a geophysical origin rather than a random scatter. There are 4 days (DOYs 92042, 95080, 95347, and 95352) for geomagnetically quiet and another 4 days (DOY 92033, 92034, 92130, and 92132) for geomagnetically active conditions. During the geomagnetically quiet days, the maximum winds of WINDII and WACCM-X are similar, while for the geomagnetically active days the maximum winds of WINDII are larger than those of WACCM-X by 100–200 m/s. It seems that WINDII winds have a stronger response to geomagnetic activity than WACCM-X winds but the agreement between the two is still remarkable.

4. Discussion and Conclusions

The WINDII observations reported upon here confirm and extend the original observations by Shepherd and Shepherd (2018) of a wind wall with extreme velocity reversals to westward in the zonal wind at 120–250 km altitude between the geographic longitudes of 100–200° and latitudes of 60–70°S. It also occurs in the Northern Hemisphere at the same latitude and altitude range but from 200° to 340° in longitude. The WINDII data only reach 72°S/N, so there are no observations poleward of those latitudes. This is consistent with the midlatitude study by Zhang and Shepherd (2008), who described “extreme longitudinal disturbances” in WINDII winds on days in 1994, 1996, and 1997, but at 40° latitude. The WINDII results also agree with the observation by Dhadly et al. (2018) that the northern polar cap winds are greatly enhanced during the summer solstice, but it should be noted that the Dhadly et al. paper incorporate WINDII winds.

In order to extend our understanding of the wind wall phenomenon, the present authors have made use of model results for the same time periods as WINDII for the recently developed WACCM-X model. The model has provided a self-consistent solution of global electrodynamics, which is different from other numerical model. The zonal winds from WINDII observations and WACCM-X simulations at high latitude for different solar radio flux, IMF, and geomagnetic conditions are compared. Both have good consistency in wind pattern and response to F10.7 and Ap. There has been a significant number of studies about the dependence of high-latitude winds on the IMF. Richmond et al. (2003), Kwak and Richmond (2014), and Huang et al. (2017) found wind generally flow westward for positive *By*. The present study also revealed a similar dependence. At UT 16:00, DOY 92130, *Bz* increased from −5.7 to 14.6 nT, during the same time period the wind velocity increased in magnitude from −100 to −400 m/s.

This clear connection of the thermospheric wind reversal to the IMF influence confirms an influence of coupling of the IMF to the magnetospheric magnetic field, perhaps through magnetic reconnection. This suggests the need for studies at latitudes higher than are available from WINDII, and so it is planned that these be explored in future studies.

This investigation leads to the following main conclusions:

1. WINDII observations and WACCM-X simulations are in generally good agreement in describing the wind wall except some difference for the pattern of the wall. For WINDII, the wall extends to larger longitude ranges, and the velocities of the westward wind are higher than those of WACCM-X, especially during geomagnetic storms.
2. The appearance of a wind wall depends on the solar radio flux and geomagnetic activity. Under low solar radio flux and geomagnetically quiet conditions, neither WINDII nor WACCM-X shows the wind wall. For high solar radio flux and geomagnetically active period, the wall is obvious, and the westward wind in the wall is extremely strong.
3. A good correlation of zonal wind and the 3-hourly ap diurnal variation is shown by WINDII observations for most geomagnetically active days investigated in present study. The correlation between WACCM-X zonal wind and the 3-hourly ap is weaker.
4. During geomagnetically quiet periods, the wind magnitudes of WINDII and WACCM-X are similar while WINDII winds are much stronger than WACCM-X for geomagnetically active periods. It is concluded that WINDII winds have a stronger response to geomagnetic activity than those in the WACCM-X model.

Acknowledgments
The authors are grateful to the WINDII team for providing excellent measurements. The WINDII project was sponsored by the Canadian Space Agency and the Centre National d'Etudes Spatiales of France, in collaboration with NASA. Science analysis was supported by the Natural Sciences and Engineering Research Council of Canada. WINDII data are available from the Canada Open Data Portal (https://open.canada.ca/en/open-data). The authors also acknowledge the essential contributions by the many members of the WACCM, CAM, and CESM development teams. WACCM-X is an open-source community model, and its source code and results are publicly available at the NCAR website. Model simulations used in this paper are run on the Niagara supercomputer of SciNet, and the authors thank the supporters for their help running the model. Shushi Liu specially thanks the China Scholarship Council and the National Nature Science Foundation of China (41604131, 41874183, and 41474131) for their sponsorship.

References

Cho, Y.-M., & Shepherd, G. (2015). Resolving daily wave 4 nonmigrating tidal winds at equatorial and midlatitudes with WINDII: DE3 and SE2. *Journal of Geophysical Research: Space Physics*, *120*, 10,053–10,068. https://doi.org/10.1002/2015JA021903

Dhadly, M. S., Emmert, J. T., Drob, D. P., Conde, M. G., Doornbos, E., Shepherd, G. G., et al. (2018). Seasonal dependence of geomagnetic active-time northern high-latitude upper thermospheric winds. *Journal of Geophysical Research: Space Physics*, *123*, 739–754. https://doi.org/10.1002/2017JA024715

Drob, D. P., Emmert, J. T., Crowley, G., Picone, J. M., Shepherd, G. G., Skinner, W., et al. (2008). An empirical model of the Earth's horizontal wind fields: HWM07. *Journal of Geophysical Research*, *113*, A12304. https://doi.org/10.1029/2008JA013668

Emmert, J. T., Drob, D. P., Shepherd, G. G., Hernandez, G., Jarvis, M. J., Meriwether, J. W., et al. (2008). DWM07 global empirical model of upper thermospheric storm-induced disturbance winds. *Journal of Geophysical Research*, *113*, A11319. https://doi.org/10.1029/2008JA013541

Gault, W. A., Thuillier, G., Shepherd, G. G., Zhang, S. P., Wiens, R. H., Ward, W. E., et al. (1996). Validation of O (1S) wind measurements by WINDII: The Wind Imaging Interferometer on UARS. *Journal of Geophysical Research*, *101*(D6), 10,405–10,430. https://doi.org/10.1029/95JD03352

Heelis, R. A., Lowell, J. K., & Spiro, R. W. (1982). A model of the high-latitude ionospheric convection pattern. *Journal of Geophysical Research*, *87*(A8), 6339–6345. https://doi.org/10.1029/JA087iA08p06339

Huang, T., Lühr, H., Wang, H., & Xiong, C. (2017). The relationship of high-latitude thermospheric wind with ionospheric horizontal current, as observed by CHAMP satellite. *Journal of Geophysical Research: Space Physics*, *122*, 12,378–12,392. https://doi.org/10.1002/2017JA024614

Hurrell, J. W., Holland, M. M., Gent, P. R., Ghan, S., Kay, J. E., Kushner, P. J., et al. (2013). The Community Earth System Model: A framework for collaborative research. *Bulletin of the American Meteorological Society*, *94*(9), 1339–1360. https://doi.org/10.1175/BAMS-D-12-00121.1

Kwak, Y. S., & Richmond, A. D. (2007). An analysis of the momentum forcing in the high-latitude lower thermosphere. *Journal of Geophysical Research*, *112*, A01306. https://doi.org/10.1029/2006JA011910

Kwak, Y. S., & Richmond, A. D. (2014). Dependence of the high-latitude lower thermospheric wind vertical vorticity and horizontal divergence on the interplanetary magnetic field. *Journal of Geophysical Research: Space Physics*, *119*, 1356–1368. https://doi.org/10.1002/2013JA019589

Liu, H.-L., Bardeen, C. G., Foster, B. T., Lauritzen, P., Liu, J., Lu, G., et al. (2018). Development and validation of the whole atmosphere community climate model with thermosphere and ionosphere extension (WACCM-X 2.0). *Journal of Advances in Modeling Earth Systems*, *10*(2), 381–402. https://doi.org/10.1002/2017MS001232

Marsh, D. R., Mills, M. J., Kinnison, D. E., Lamarque, J.-F., Calvo, N., & Polvani, L. M. (2013). Climate change from 1850 to 2005 simulated in CESM1 (WACCM). *Journal of Climate*, *26*(19), 7372–7391. https://doi.org/10.1175/JCLI-D-12-00558.1

Neale, R., Richter, J., Park, S., Lauritzen, P., Vavrus, S., Rasch, P., & Zhang, M. (2013). The mean climate of the Community Atmosphere Model (CAM4) in forced SST and fully coupled experiments. *Journal of Climate*, *26*(14), 5150–5168. https://doi.org/10.1175/JCLI-D-12-00236.1

Richmond, A. D., Lathuillere, C., & Vennerstroem, S. (2003). Winds in the high-latitude lower thermosphere: Dependence on the interplanetary magnetic field. *Journal of Geophysical Research*, *108*(A2), 1066. https://doi.org/10.1029/2002JA009493

Rienecker, M. M., Suarez, M. J., Gelaro, R., Todling, R., Bacmeister, J., Liu, E., et al. (2011). MERRA: NASA's modern-era retrospective analysis for research and applications. *Journal of Climate*, *24*(14), 3624–3648. https://doi.org/10.1175/JCLI-D-11-00015.1

Shepherd, G. G., & Shepherd, M. G. (2018). High-latitude observations of a localized wind wall and its coupling to the lower thermosphere. *Geophysical Research Letters*, *45*, 4586–4593. https://doi.org/10.1029/2018GL077722

Shepherd, G. G., Thuillier, G., Cho, Y.-M., Duboin, M.-L., Evans, W. F. J., Gault, W. A., et al. (2012). The Wind Imaging Interferometer (WINDII) on the Upper Atmosphere Research Satellite: A 20 year perspective. *Reviews of Geophysics*, *50*, RG2007. https://doi.org/10.1029/2012RG000390

Shepherd, G. G., Thuillier, G., Gault, W. A., Solheim, B. H., Hersom, C., Alunni, J. M., et al. (1993). WINDII, the Wind Imaging Interferometer on the Upper Atmosphere Research Satellite. *Journal of Geophysical Research*, *98*(D6), 10,725–10,750. https://doi.org/10.1029/93JD00227

Solomon, S. C., & Qian, L. (2005). Solar extreme-ultraviolet irradiance for general circulation models. *Journal of Geophysical Research*, *110*, A10306. https://doi.org/10.1029/2005JA011160

Zhang, S. P., & Shepherd, G. G. (2008). Extreme longitudinal disturbances in the mesosphere and thermosphere observed with the Wind Imaging Interferometer on UARS. *Geophysical Research Letters*, *35*, L16802. https://doi.org/10.1029/2008GL034352